Plasma Sources Science and Technology

PAPER • OPEN ACCESS

Breakdown development in a nanosecond pulsed dielectric barrier discharge in humid air in plane-to-plane geometry

To cite this article: Paolo F Ambrico *et al* 2023 *Plasma Sources Sci. Technol.* **32** 095008

OPEN ACCESS
IOP Publishing
Plasma Sources Science and Technology
Plasma Sources Sci. Technol. **32** (2023) 095008 (14pp)
https://doi.org/10.1088/1361-6595/acf6df

Breakdown development in a nanosecond pulsed dielectric barrier discharge in humid air in plane-to-plane geometry

Paolo F Ambrico[1,*], Domenico Aceto[1], Lorenzo Ibba[2], Xin Yang[3], Giorgio Dilecce[1], Marianna Ambrico[1], Ivo Furno[2] and Igor V Adamovich[3]

[1] CNR, Istituto per la Scienza e Tecnologia dei Plasmi, Sede di Bari, Via Amendola 122/D, Bari, Italy
[2] Swiss Plasma Center (SPC), École Polytechnique Fédérale de Lausanne (EPFL), CH-1015 Lausanne, Switzerland
[3] Department of Mechanical and Aerospace Engineering, The Ohio State University, Columbus, OH 43210, United States of America

E-mail: paolofrancesco.ambrico@cnr.it

Received 28 May 2023, revised 8 August 2023
Accepted for publication 5 September 2023
Published 15 September 2023

Abstract

We used the ns electric field induced second harmonic (EFISH) generation diagnostic to measure the electric field evolution in a 200 ns pulse, dielectric barrier, plane-to-plane discharge in humid air, on the time scale shorter than the laser pulse duration. Plasma imaging by an ICCD camera detected a uniform evolution of the discharge emission during the breakdown. Spectroscopic measurements tracked the N_2 second positive and first negative systems to infer the reduced electric field (E/N) evolution. EFISH measurements showed the electric field persistent during the entire HV pulse, with the residual field between pulses and the field inversion at the start and end of the HV pulse. The experimental data are consistent with the simulations, with the electron attachment and negative ion kinetics incorporated. The modeling predictions indicate that the rapid electron density decay due to attachment and recombination is the dominant factor sustaining the electric field in the plasma after breakdown. Spectroscopic E/N determination showed the time evolution at variance with the EFISH measurements, which may be due to the electron attachment and non-locality of the EEDF. Possible explanations are discussed.

Keywords: EFISH, nanosecond pulsed discharge, atmospheric pressure DBD

(Some figures may appear in colour only in the online journal)

* Author to whom any correspondence should be addressed.

1. Introduction

The application of low-temperature plasma to several biological systems has in the last decades attracted the attention of researchers in the field [1–8]. Several physical agents interact with biological tissues when plasma treatment is applied. One that should have major importance is the local electric field produced by the plasma.

Electric field measurements in plasmas using electric field induced second harmonic (EFISH) generation and ultrashort pulsed lasers [9, 10] are increasingly common. This method has been employed in various plasma environments, including ionization wave plasmas in air, nitrogen, hydrogen and hydrocarbon flames, as well as Ar and He plasma jets [11–16]. This non-intrusive technique provides time- and space- resolved electric field vector components with sub-ns temporal resolution.

Although the measurements mentioned earlier utilized fs and ps lasers, the possibility of conducting steady-state electric field measurements in ambient air using ns pulse duration lasers was demonstrated more than four decades ago [17]. The main drawback of using readily available ns pulse duration Nd:YAG lasers for EFISH diagnostics is their limited temporal resolution, usually around 10 ns. This timeframe often exceeds the necessary duration for crucial processes like breakdown development, plasma self-shielding, and ionization wave propagation in high-pressure pulsed plasmas. To resolve the temporal variation of the electric field throughout the duration of a ns laser pulse, we have followed the approach reported in [18]. In this way the temporal resolution of the measurements is limited solely by the time response of the detector and oscilloscope.

EFISH can be performed with high temporal resolution (potentially sub-ns) using a ns pulse duration laser. In such a way in our experiments we were able to follow the evolution of the electric field in a nanosecond discharge, running at a repetition rate of 1 kHz, in humid air. The gas mixture used was selected being representative of the typical condition of plasma treatment of biological tissues.

The EFISH measurements were compared with a electric field derived by a discharge model simulation, to understand the processes involved in the development of the electric field.

It is worth to point out that usually in the literature the electric field is indirectly measured by applying optical emission spectroscopy and following the emission of the first negative and second positive systems (SPSs) of the nitrogen molecules [19]. The fact that such measurements can only be performed during the plasma-on phase of the treatment, is a strong limitation in processes where the plasma is amplitude modulated to keep the gas temperature as close as possible to room one, making this method most of the cases not useful. Nevertheless a comparison of the estimated E/N measurements by spectroscopic methods and direct measurements by EFISH was conducted during the nanosecond pulse using spectroscopic observation performed by intensified charge-coupled device (ICCD) kinetics series spectra images that gives us the opportunity of obtaining the nanosecond time resolution for spatially resolved spectra (with resolution potentially down to 13 μm).

2. Experimental

The schematic of the experimental apparatus used for ns EFISH generation diagnostic is shown in figure 1. Briefly, the fundamental 1064 nm output of a ns pulse Nd:YAG laser (Opotek, pulse duration 7 ns full width at half maximum (FWHM), pulse repetition rate up to 20 Hz, $\phi = 3$ mm, 'flat top' beam profile) is directed between two parallel plane circular electrodes. The laser beam profile guarantees that the Rayleigh length is longer than the interaction zone and coherence length, thus excluding one of the possible conditions causing the distortion of the EFISH signal [20]. The polarization plane of the laser beam can be adjusted by a zero-order half-wave plate (Thorlabs WPH05ME-1064) in a rotation mount. The laser beam is focused between the electrodes by a 50 cm focal distance lens, as shown in figure 1.

The stray second harmonic signal generated within the focusing lens is blocked by an 850 nm long pass filter (Thorlabs FGL850M). After the electrodes, the laser beam contains the second harmonic signal beam at 532 nm, generated by the electric field between the electrodes, along with the 1064 nm pump beam. The second harmonic beam is separated from the remaining pump beam by a Pellin Broca prism (Thorlabs ADBU-10) and detected by a photomultiplier tube (Hamamatsu Fast PMT, model H10721-20, nominal rise time 0.57 ns), as shown in figure 1. A thin film polarizer (Thorlabs PVISE050-A) in a rotation mount is placed before the PMT, to isolate the vertically polarized EFISH signal, generated by the vertical electric field component between the electrodes. A narrow band pass filter (Thorlabs FL532-10, 1" Laser Line Filter, CWL $= 532 \pm 2$ nm, FWHM $= 10 \pm 2$ nm) in front of the PMT blocks the stray light and the pump laser beam reflections. The PMT gain is selected to ensure its linearity over the entire range of the measured electric field. A reflection of the 1064 nm beam, controlled by an iris diaphragm, is detected by a photodiode (AlphaLas Fast Photodiode UPD-200-UP, nominal rise time $<$175 ps), to monitor the time-resolved laser pulse intensity. The laser pulse energy is stable within 5%. The alignment of the optical system is done using the second harmonic generated by the optical parametric oscillator (OPO), which is subsequently removed. The electrodes are circular brass plates 20 mm in diameter. Each electrode is covered by a CoorsTek 99.5% alumina ceramic plate 0.668 mm thick, used as a dielectric barrier. The gaps between the electrodes and the ceramic plates are filled with a silicone adhesive (Model/Make). The discharge gap, i.e. the distance between the ceramic plates, is 1.75 mm. The electrodes are held in a 3D-printed plastic electrode assembly, mounted on a vertical translation stage, such that the relative position of the laser beam in the discharge gap can be varied. The process gas is Pure Air (Rivoira, 5.0), that is flowing at 2 slm through an MKS flowmeter controlled by an MKS PR-4000. The gas can either flow directly into the chamber, or passing through a glass bubbler (capacity 500cc) to produce humid air. At the normal laboratory condition, i.e. 21 °C and atmospheric pressure, the RH of the humid air is about 75%.

The discharge electrodes are powered by a custom-made ns pulse generator based on a solid state high voltage switch

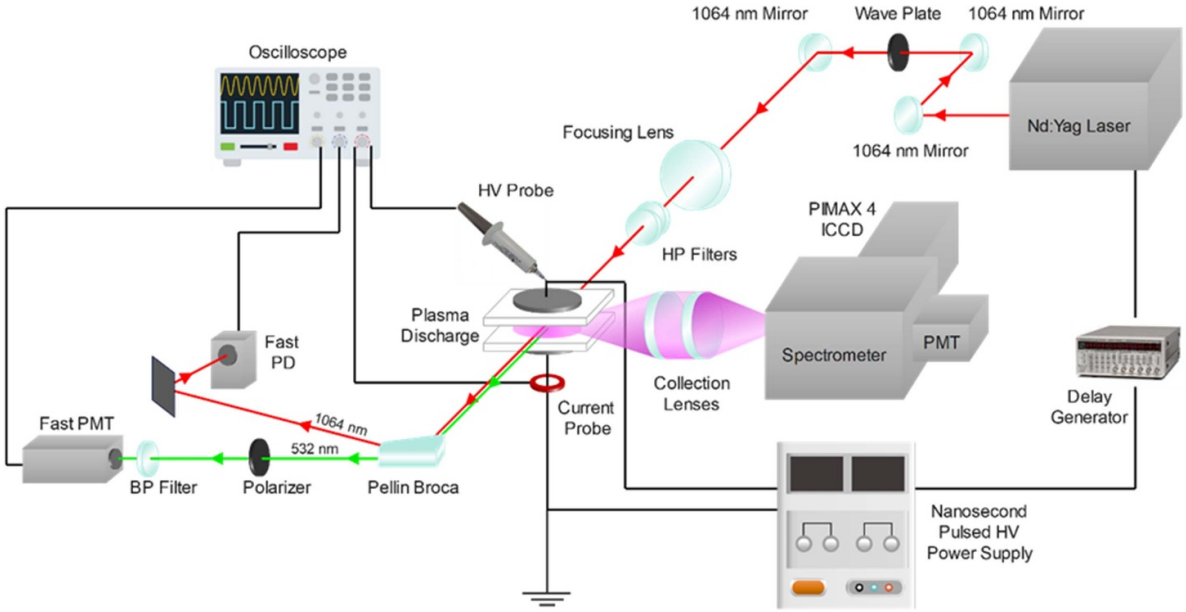

Figure 1. Experimental setup schematics.

Behlke HTS 241-20-GSM, able to produce the positive polarity voltage pulses with peak voltage up to 24 kV, pulse duration of 200 ns, voltage rise/fall time of 50 ns, and operating at a maximum pulse repetition rate of 1 kHz. The discharge was generated in the humid air. The flashlamps and the Q-switch of the laser, as well as the high-voltage pulse generator, are triggered by ns pulse generator internal cards and an external delay generator (HP8112 A Pulse generator) to finely tune the laser pulse delay with steps of 0.1 ns. To measure the time-varying electric field in the discharge over a time interval longer than the laser pulse duration, the time delay of the laser pulse relative to the high-voltage pulse is varied. The time delay variation, up to several hundred ns, does not affect the laser pulse energy. The pulse voltage waveform is monitored by the high voltage (HV) pulse generator internal electronics using an integrated high-voltage probe Hivolt model PHV4002-3 (voltage up to 40 kV, bandwidth 100 MHz) and measured at the high voltage electrode by a Tektronix P6015A probe (voltage up to 40 kV peak, Bandwidth 75 MHz, rise time 4.7 ns). Current delivered at the discharge is measured by a Magnelab CT-c1.0 Rogowski coil current monitor (rise time 0.7 ns) on the ground electrode. The voltage waveform, the photodiode signal, and the PMT signal are measured by a Keysight Infiniivision MSOX 6004 A Mixed Signal Oscilloscope (1 Ghz Bandwidth, 20Gsample/s).

Optical emission spectroscopy was performed by collecting the light from the plasma with two 30 cm focal length UV grade quartz lenses imaging (1:1) the discharge gap on the entrance slit of a monochromator. The imaged area is limited by the entrance slit and can reach a maximum dimension of 3 (l) $\times$ 5 (h) mm^2. The light is spectrally resolved by a 30 cm spectrometer (Acton Spectra Pro 2300), equipped with a multiple-grating turret with a 300/600/1200 grooves $\times$ mm^{-1}, blazed at 300 nm. The spectrum is acquired with a Princeton Instruments PI-MAX4 1024i CCD camera equipped with a 1024 $\times$ 1024 pixel sensor (size 12.8 μm, active area 13.1 $\times$ 13.1 mm^2). One CCD image of a spectrum covers a range of approximately 144/65/30 nm respectively for the three different gratings. The intensities of the emission spectra acquired by the ICCD detector were spectrally and intensity corrected through calibration and halogen lamps.

Broadband plasma images are taken by the same UV-grade optical setup with the addition of a UV gage objective to magnify the image and a dove prism to rotate from horizontal to vertical the 2 cm x 1.75 cm image of the discharge so that it is aligned with the entrance of the monochromator. ICCD gate was varied from 3 ns to 120 ns.

3. Results

3.1. Discharge characteristics

Figure 2 displays typical single-shot voltage-current- PMT waveforms of the discharge.

The discharge usually occurs with a delay of approximately 90 ns after the high voltage pulse onset, as shown by the current impulse displayed in the second trace. Two current peaks were detected, the first one at the onset of the HV pulse the second one at the end. The typical amplitude of the current pulse observed at the onset was of the order of 6 A, and 2A at the switch off. For a single current shot we measured the full width at half maximum of about 15 ns for both current peaks. As well as following the current waveform, the discharge formation can be evidenced by the PMT signal that captures the SPS (0,2) band taken through the monochromator.

In our discharge we reached the conditions of the reduced overall jitter of the cathode- and anode- directed current, respectively, at the onset and switch-off of the HV pulse, with respect to the leading edge of the HV pulse. Figure 3 shows the measured jitter distribution evaluated by following the

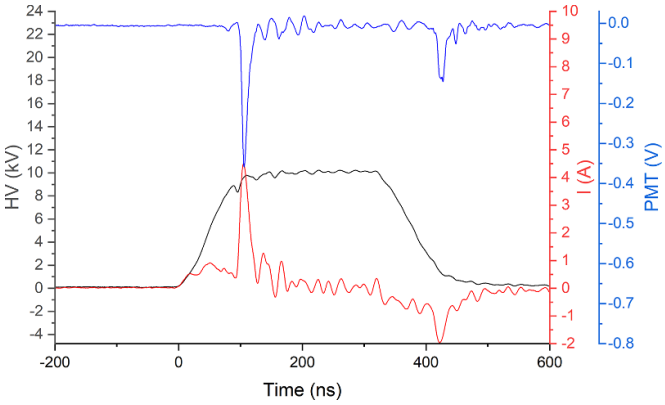

Figure 2. Typical voltage (black), current (red) and SPS(0,0) band emission taken through the monochromator by means of the fast PMT.

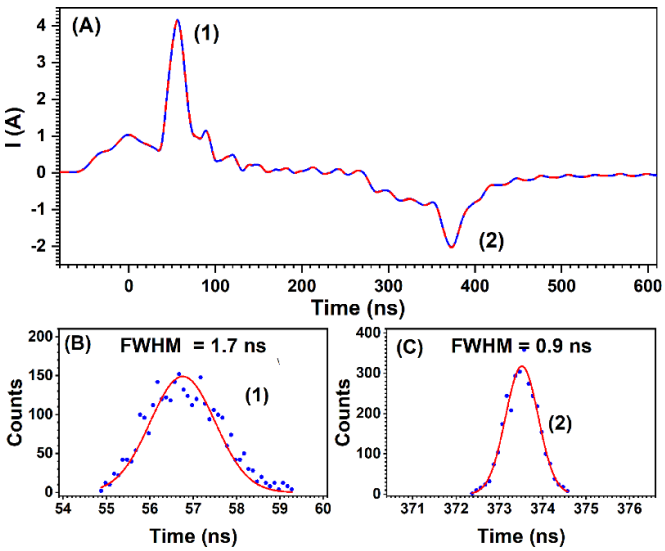

Figure 3. Current jitter with respect to the rising edge of the high voltage pulse.

current peak maximum over 3500 single shots, that is more than 10 times the typical number of shots used for EFISH measurements.

The current jitter follows a normal distribution with a measured FWHM of about 1.7 ns for the current peak (1) and 0.9 ns for the current peak (2). The lower value of the jitter for the second peak can be justified by a more stabilized condition with respect to the discharge onset. Moreover, events with bigger jitter or no current signals were not detected if a pre-warm up procedure (consisting of a run of 500 shots) was performed prior to the measurements. The measured jitter could allow a sufficiently precise timing of all measurements and recording sequences of statistically averaged imaging/spectroscopic measurements and current voltage characteristics.

Another relevant figure is the jitter between the laser output pulse and the voltage pulse. The jitter was estimated by triggering the acquisition on HV pulse. We obtained a normal distribution, as shown in figure 4, with an estimated FWHM of 3 ns. This can be attributed to the trigger electronic chain

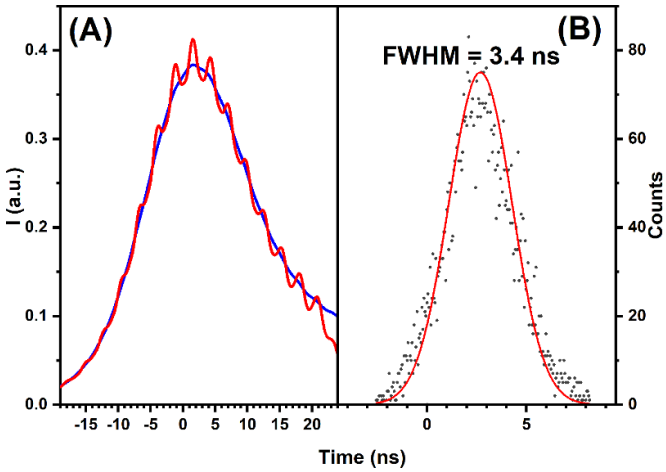

Figure 4. Laser jitter with respect to the HV rising edge. (A) Averaged waveforms obtained by simple average of 6000 single waveforms (Blue line) and the jitter corrected averaged waveform. (B) Distribution of peak position with time and the corresponding normal distribution showing a FWHM of 3.4 ns.

that is used to perform the measurements. To evaluate the possible effects on the EFISH measurements of the electronics jitter on the time averaged signals the jitter distribution was evaluated also for the laser trigger chain. Several thousands of single fundamental laser shots were acquired by means of the fast photodiode triggering the oscilloscope on the HV rising edge as for the current. The results are shown in figure 4. In panel (A) the time averaged (over 6 K acquisitions) and the jitter corrected averaged over 6 K waveforms are shown together. The multimode fine structure of the laser pulse is completely recovered in the jitter-corrected signals while it is smoothed out in the simple averaged signal. We must point out that even if the normal distribution of the jitter delays has a FWHM of 3 ns we do not observe the laser jitter effect on the measured signal since we trigger the acquisition on the fast photodiode and not on the HV pulse rising edge. Finally, the timing jitter between the laser traces measured by the fast photodiode and the fast PMT was estimated to be sub-nanosecond, making it a minor source of uncertainty. Nevertheless, the measured jitter suggests that in the worst scenario with the current electronic chain processes faster than 4 ns, will be mainly smoothed by the external laser trigger electronic jitter even though the shape will be preserved. Anyway, this is sufficient for the time scale of the processes that we want to follow. With the current electronics we could improve the time resolution by a more time and resource consuming approach consisting in the acquisition of a statistically significant single shot voltage, current, photomultiplier and photodiode signals and postprocessing recovering the jitter corrected one (time binning).

Figure 5(A) shows a single-shot broadband plasma emission image taken during the discharge pulse, using a camera gate of 50 ns. The discharge images were taken using humid and dry air. It is readily apparent that the plasma in humid air is diffuse, and the emission fills the entire discharge gap, with no sign of isolated filaments, such as in the case of dry air. The diffuse character of the humid air discharge is also

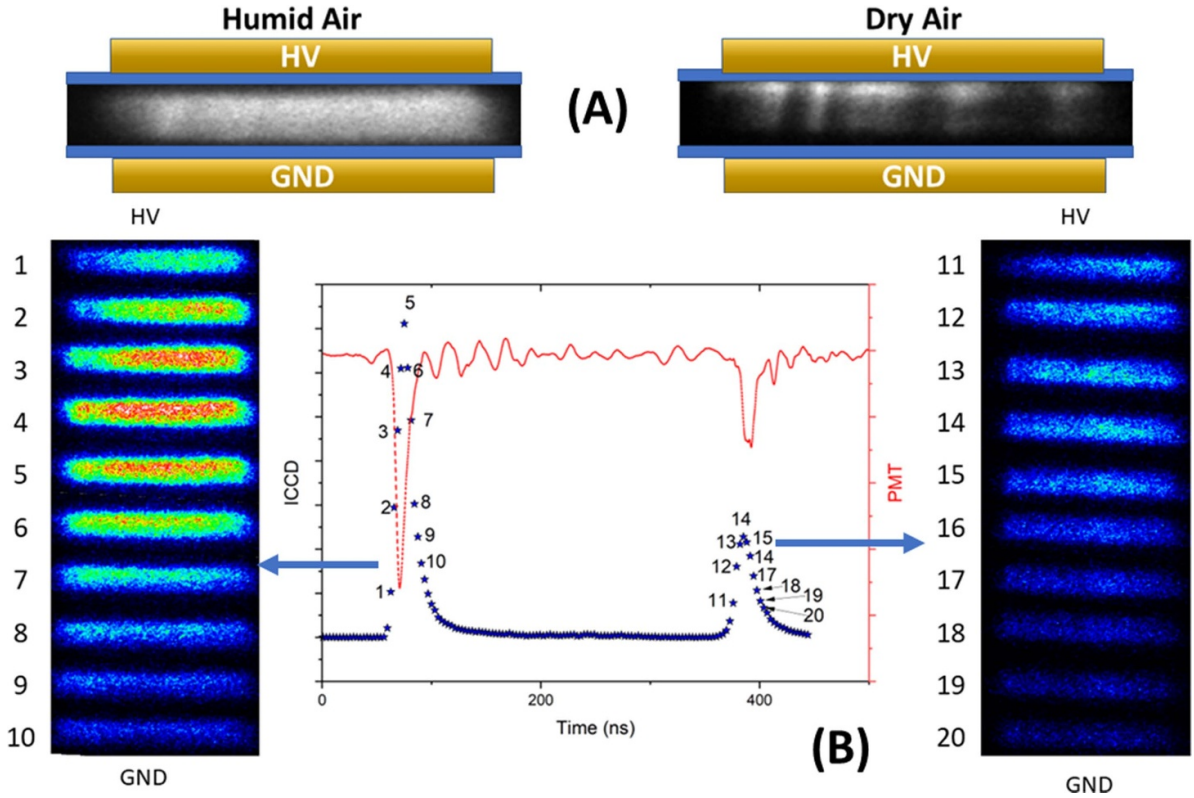

Figure 5. (A) Collage of the single-shot plasma emission images taken during the discharge pulse, using the camera gate of 50 ns in humid and dry air. (B) Kinetic images with a fixed gate of 3 ns during the 1st and 2nd discharge pulse emission in humid air at the gate position highlighted in the PMT/ICCD intensities plot.

confirmed by the single shot images of an ICCD kinetic series taken with a camera gate of 3 ns (panels (B1), (B2)). This suggest a key role of water vapor in the plasma dynamics of the discharge. Comparison of the single shot PMT signals and the full vertical binning emission intensities shows a satisfactory agreement such that we conclude that the current jitter with respect to the HV rising edge is not affecting the images and consequently the spectra acquired by ICCD.

3.2. EFISH measurements

The electric field is determined from the time-resolved PMT and photodiode waveforms, $I^{(2\omega)}(t)$ and $I^{(\omega)}(t)$, respectively, using the following equation (1),

$$E_{\text{ext}}(t) = A\,\frac{\sqrt{I^{(2\omega)}(t)}}{I^{(\omega)}(t)} \tag{1}$$

where A is a calibration constant that takes into account all the transfer functions of the signals. The stray phase shift between the PMT (second harmonic) and photodiode (pump laser) signals is determined from the measurement of the steady-state Laplacian electric field when the ratio of the square root of the PMT waveform and the photodiode waveform should be constant, as discussed in [1].

Figure 6 reports a comparison between the normalized and averaged square root of the PMT (EFISH signal) and photodiode waveforms (1064 nm laser beam), respectively, over

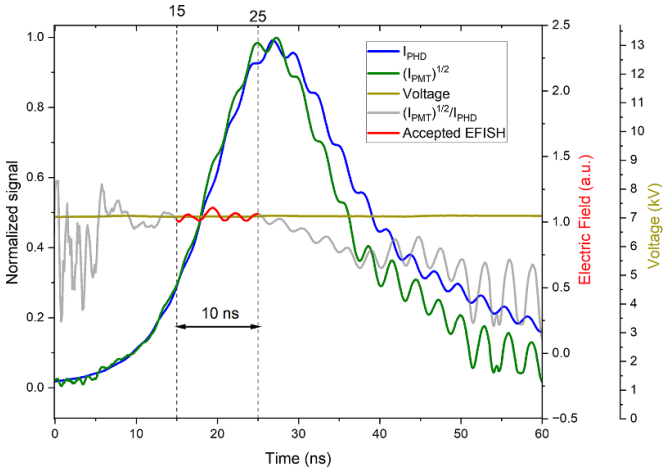

Figure 6. Normalized square root of the PMT signal measured at a constant electric field overlapped with the photodiode signal (both signals averaged over 256 laser shots), and their ratio. The time interval where the time-accurate EFISH data can be monitored is labelled. P = 760 torr, laser pulse energy 9 mJ.

256 laser shots. All the measurements were taken in air at 1 atm with a constant Laplacian electric field and a laser pulse energy of 9 mJ. No laser induced breakdown in air was observed. To avoid smoothing out the structures, the waveforms were triggered on the fast photodiode's rising edge. The observed ratio of the two waveforms, which is proportional

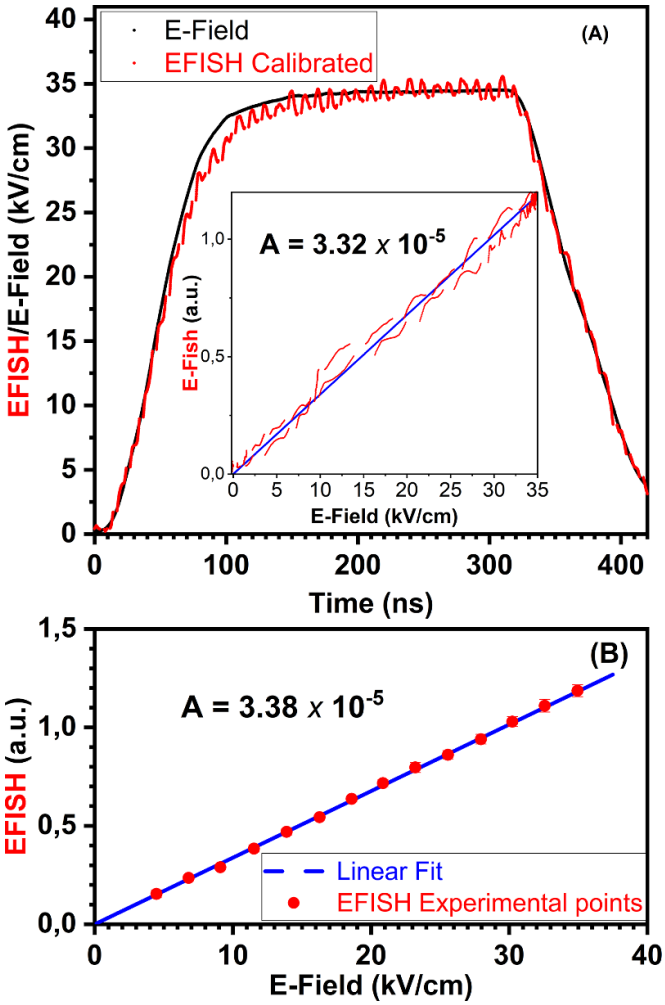

Figure 7. Calibration of EFISH signals using a voltage pulse (A) or a constant voltage (B). The resulting calibration factors A are displayed in the figures.

to the electric field (see equation (1)), remained constant for almost 10 ns during a significant fraction of the laser pulse duration. This finding indicates that it is possible to measure the temporal variation of electric field during the laser pulse, $E_{\text{ext}}(t)$.

Calibration is obtained by measuring the Laplacian electric field produced by a constant voltage and a sub-breakdown voltage pulse applied to the electrodes.

This is demonstrated in figure 7, which illustrates the temporal calibration of the EFISH data by employing a Laplacian electric field pulse with a duration of about 400 ns. The electric field, generated by a sub-breakdown high-voltage pulse with a maximum peak voltage of 7 kV a pressure of 1 atm, was measured by the Tektronix P6015 (75 MHz) high voltage probe. During these measurements, the laser beam was polarized vertically at the measurement location, and the polarizer before the PMT transmitted the horizontally polarized second harmonic signal generated by the axial electric field.

The EFISH measured electric field waveforms, displayed in figure 7, were obtained by modifying the delay time between the high-voltage pulse and the laser pulse, resulting in more than 50 steps, with a delay varying from 5 ns in the rising and decreasing edges up to 10–20 ns in the plateau. The individual data sets' partially overlapping intervals were merged to create the final data sets. In figure 7 the EFISH signal is plotted against the applied electric field in the gap,

$$E_{\text{app}} = \frac{U_{\text{app}}}{d^*} \tag{2}$$

where $U_{\text{app}}(t)$ is the applied voltage, d^* is the effective gap distance used that includes the voltage drop due to the dielectric surfaces, $d^* = d + 2l/\varepsilon_r$. $d = 1.75$ mm is the air gap, $l = 0.66$ mm is the thickness of each dielectric layer, and $\varepsilon_r = 9.8$ is the relative dielectric constant of the alumina ceramic dielectric. It can be seen that the relative electric field waveform inferred from the EFISH measurements is in very good agreement with the applied voltage waveform during the voltage rise, demonstrating the temporal accuracy of the composite EFISH data. A calibration curve is then obtained by using all the EFISH raw data set vs $E_{\text{app}}(t)$ returning a calibration constant $A = 3.32 \times 10^{-5}$.

To check the accuracy of the calibration a second method was adopted by using a constant HV value and taking the EFISH mean value. The resulting calibration curve is reported in figure 7(B). The calibration constant in this case is $A = 3.38 \times 10^{-5}$ in close agreement with the one obtained using the HV voltage pulse.

The EFISH measurements during the discharge were taken at three different spatial positions displayed in the top part of figure 8.

The positions were corresponding to the maximum travel distance through the discharge achievable by the laser beam without significantly reducing the laser beam energy at the exit. We can assume that the laser in position (A) and (C) is just grazing the dielectric barriers, but due to the finite size of the laser beam the resulting electric field is a spatially integrated representation of the electric field encountered by the beam along its entire volume. The waist of the beam at the entrance of the discharge is estimated to be about 0.8 mm. In this way position (A) correspond to the closest position to the HV electrode, (B) to the middle of the gap and (C) to the closest position to the GND electrode. The delay time between the high-voltage pulse and the laser pulse was varied in more than 70 steps, with a delay varying from 5 ns in the rising and decreasing edges up to 10–20 ns in the plateau.

Figure 8 shows the EFISH data obtained in the discharge during the operation, together with the effective electric field derived from the applied voltage waveforms, and the discharge current. In both the rising and falling edges of the HV pulse from the EFISH signal undergoes a sign reversal, caused by residual surface charge accumulation on the dielectric. Since the EFISH measurements is measuring the absolute value of the electric field, the sign reversal is detected in the raw data as a signal 'dip' to the background noise level, with zero field value at the reversal point. The field sign reversal must be manually imposed at those points in accordance with the applied voltage values.

The resulting EFISH measurements (figure 8) show good agreement between the electric field evaluated from the

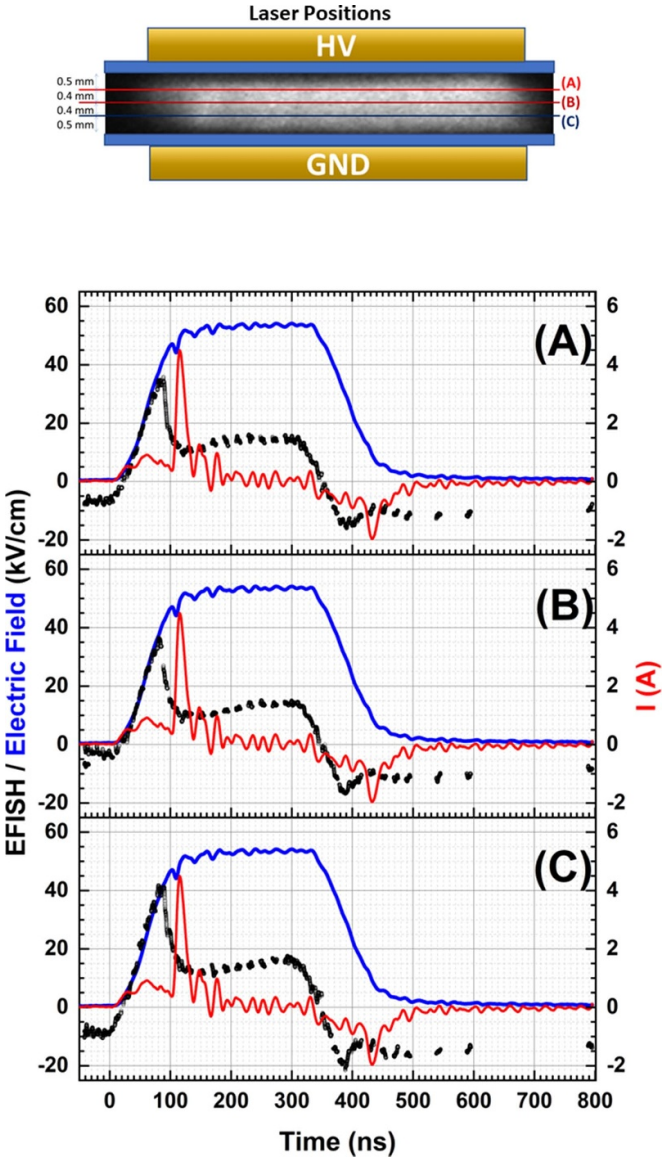

Figure 8. Time-resolved electric field in the discharge gap at 3 different vertical position shown in the top part of the figure.

voltage measurements until the breakdown, for all three cases. After the start of the breakdown the EFISH shows a quite rapid drop of the electric field in all the positions. This event is marked also by the current measurements. However, the electric-field after breakdown in all cases never reaches the zero value, but a slow rising in the field is observed till 300 ns.

3.3. Kinetic modeling

The kinetic model used in the present work is similar to the one used in [21] for the simulation of ionization wave formation and propagation in a ns pulse discharge in nitrogen in plane-to-plane geometry, which exhibits good agreement with the experimental data. Briefly, the present model incorporates the one-dimensional equations for the number densities of electrons, positive ions, and negative ions in the fluid (drift-diffusion) approximation, coupled with the Poisson equation for the electric potential. The plasma shielding due to the charge accumulation on the dielectric surfaces adjacent to the electrodes is considered. The rates of electron impact ionization and dissociative attachment to O_2, $O_2 + e \rightarrow O + O^- + e$, in humid air (3% water vapor) are calculated using Bolsig+ with Morgan database [22], vs. the reduced electric field (E/N). The rates of the three-body attachment rate to O_2, $O_2 + e + M \rightarrow O_2^- + M$, with $M = O_2$, H_2O, and N_2, are taken from [23]. An empirical fit for the ionization frequency, $\nu_{\rm ion} = \sum k_{{\rm ion},i} n_i$ ($i = N_2, O_2, H_2O$), based on the experimental data in humid air [24] is used to verify and validate the modeling predictions using the ionization frequency predicted by Bolsig+. The rates of electron-ion recombination and ion-ion neutralization are taken from [23, 25], $\beta_{ei} \approx 5 \times 10^{-6}$ cm^3 s^{-1} and $\beta_{ii} = 10^{-6}$ cm^3 s^{-1}, respectively, assuming $H_3O^+(H_2O)_n$ and O_2^- to be the dominant ions. This assumption is based on the rates of the dominant ion-molecule conversion processes. The ion mobilities are taken from [26, 27]. The electron and ion diffusion coefficients are calculated from their mobilities and temperatures using the Einstein relations [28]. The initial ion densities in the gap, before the discharge pulse, are evaluated based on the rate of ion-ion neutralization, $n_{i,0} \sim \frac{1}{\beta_{ii}\tau} = 10^9$ cm^{-3}, where $\tau = 10^{-3}$ s is the time interval between the discharge pulses. The initial electron density is considered an adjustable parameter, $n_{e,0} = 10^6$ cm$^{-3} \ll n_{i,0}$. The modeling predictions, such as the breakdown voltage and the electric field in the plasma, are weakly sensitive to the initial electron density, as long as it is much lower than the initial ion density. The initial electric field in the gap, affected by the surface charge accumulation from the previous pulse, E =2.5 kV cm^{-1}, is taken from the experimental data.

The present formulation of the model does not include the electron energy equation or Boltzmann equation for the electron energy distribution function (EEDF), such that the ionization coefficient and the charge species drift velocities are the functions of the local electric field, rather than the electron temperature or EEDF. This assumption does not account for the EEDF relaxation in a rapidly changing electric field, which limits the estimated time resolution of the modeling predictions, $\tau_{\rm EEDF} \sim 0.01$ ns at the present conditions. The fluid model with the local ionization approximation is valid only at relatively low electric fields and electric field gradients, such that (i) the electron energy gained over the mean free path is much lower compared to the ionization energy, and (ii) the electric field variation over the mean free path is insignificant [28]. At the present conditions, this gives $E \lesssim 200\ \frac{\rm kV}{\rm cm}$ and $E\left(\frac{{\rm d}E}{{\rm d}x}\right)^{-1} \gtrsim 10^{-4}$ cm.

The accurate high-fidelity predictions of the electron density and the ion composition in the plasma in humid air would require incorporating the air plasma chemistry to predict the generation of O atoms, ozone, and nitric oxides; the equations for multiple positive and negative ions, including water vapor cluster ions; and a large number of ion-molecule reactions. However, the main objective of the kinetic modeling in the present work is rather different, that is to identify the dominant kinetic processes controlling the electric field in the ns pulse

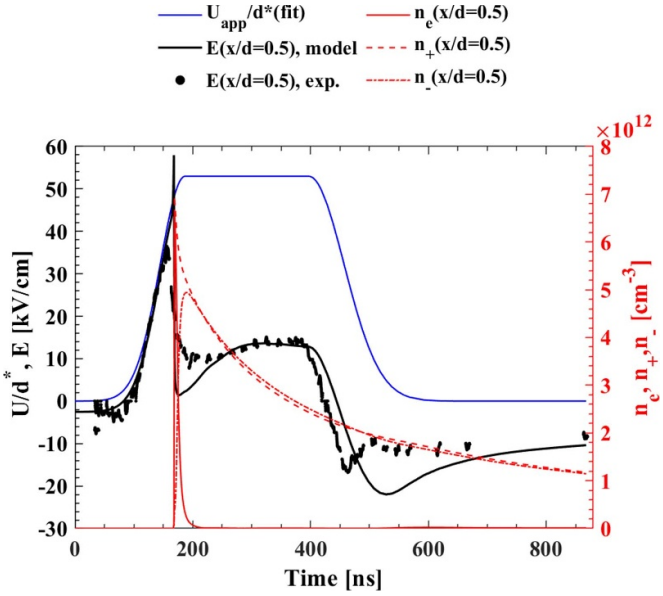

Figure 9. EFISH measurements (black dots) with the model calculations on the gap centerline: Electric field ($E(x/d = 0.5)$), applied electric field (U/d^*), discharge current (I), electron (n_e), positive (n_+) and negative (n_-) ion densities. The applied voltage waveform is the fit to the experimental data, plotted in figure 8.

discharge gap in humid air after breakdown. The present analysis is expected to be followed up by the high-fidelity simulations, which can be used for their validation and assessment of the predictive capability.

Figure 9 reports the model predictions together with the measured electric field (at the position (B)) and the applied electric field in the gap, used in the model calculation, that is derived from a fit of the measured applied voltage by means of equation (2). Figure 10 also compares the electric field measured on the gap centerline, $E\left(\frac{x}{d} = 0.5\right)$, with the modeling predictions. The number densities of electrons, positive ions, and negative ions predicted by the model are also plotted in the figure.

From figure 9, it can be seen that, when the applied voltage increases, the field in the gap follows it, as expected. Since the initial electron and ion densities in the gap are very low, the field in the gap remains Laplacian, except for the offset caused by the charge accumulation on the dielectric surfaces during the previous discharge pulse. Right before breakdown, which results in a sudden electron density increase and the electric field drop, the electric field exhibits a pronounced overshoot, on a sub-ns time scale (see figure 9). This overshoot, which was measured in the previous electric field measurements in a diffuse ionization wave in ambient air [13] and in a ns pulse discharge in nitrogen [21] using ps EFISH, is not detected by the present ns EFISH. Comparison with the modeling predictions demonstrated that the overshoot is caused by the formation of a transient ionization wave in the plasma [21]. The apparent absence of the overshoot in the present experimental data may be due to the limited time resolution of the present EFISH diagnostic but may also be caused by the sub-ns jitter of the breakdown moment pulse-to-pulse.

From figure 9, it is apparent that the model overpredicts the breakdown voltage, such that the breakdown occurs later in time, compared to the experimental data. In the modeling calculation plotted in figure 9, we used the empirical fit for the ionization frequency in humid air [24]. In comparison, the use of the ionization frequency predicted by Bolsig+, which is lower compared to that suggested in [24] at $E/p > 50$ V cm^{-1} Torr results in an even more significant breakdown voltage overprediction. This illustrates that the predictive capability of kinetic models based on the steady-state, two-term expansion solution of the Boltzmann equation for ns pulse discharge plasmas is rather limited.

The most striking difference between the present data and the previous electric field measurements in nitrogen [21] is that the electric field after breakdown does not fall to near zero (detection limit), but remains at 30%–40% of the breakdown value, following a gradually rising plateau (see figure 9). The comparison of the modeling predictions in nitrogen and humid air demonstrates clearly that this difference is caused by the rapid electron attachment (primarily three-body attachment) and a significantly faster electron-ion recombination in the latter case. The reason for this behavior is readily apparent. In humid air, the electron/positive ion plasma formed during breakdown is rapidly converted to the negative ion/positive ion plasma, due to the rapid electron density decay, on the time scale of ~10 ns (see figure 9). This greatly reduces the mobility of the negative charges, such that the plasma self-shielding due to the charge separation, which would otherwise occur within a few ns, is partially inhibited. This results in a less significant accumulation of the electrons on the anode-adjacent dielectric wall, which would otherwise create a polarization field across the entire gap to balance the applied electric field, as occurs in the nitrogen plasma [21]. Basically, if the electron decay occurs on the time scale shorter than the characteristic time for the electron drift to the anode (i.e. within a few nanoseconds), the flux of the negative charges to the anode and the plasma self-shielding are greatly retarded, due to the much lower negative ion mobility.

In addition, the drift of the positive ions toward the wall adjacent to the grounded electrode (cathode) during the remainder of the pulse, driven by a very strong field in the cathode sheath, generates the negative space charge in the rest of the discharge gap. In the electron-ion plasma, this negative space charge would be rapidly dissipated by the drift of the highly mobile electrons. However, in the ion-ion plasma the space charge persists for a much longer time, due to the much lower mobility of the negative ions. This effect is responsible in the gradual increase of the electric field in the gap, after the initial rapid fall caused by the breakdown (see figure 9). In nitrogen at the same conditions, the model predicts the electric field to fall to zero after breakdown, as was also predicted in [21] at a lower pressure of 100 Torr, in good agreement with ps EFISH data.

Note that the kinetic model predicts a much faster reduction of the electric field after the breakdown, a few ns compared to a few tens of ns (see figure 9). The depth of the electric field 'dip', with the subsequent recovery, is also overpredicted. The reason for this difference is not fully understood, and may indicate the effect of the electric field outside the plasma (e.g. created by the surface charges accumulated on the dielectric surfaces outside of the overlapping electrodes). This would contribute into the net EFISH signal accumulated along the focused laser beam, and in particular affect its temporal variation. However, the present experimental results indicate that this is unlikely. Indeed, if the contribution of the 'stray' electric field outside the plasma were significant, the EFISH signal measured during the applied voltage reduction would not decrease to near zero (detection limit) at the 'zero-field' (field reversal) point, when the field in the plasma becomes zero. This would create a noticeable 'jump' in the electric field data, such as observed in [29]. However, as is readily apparent from figure 9, the zero-field point is detected with confidence at $t \approx 420$ ns. A significant contribution of the 'stray' field outside of the discharge gap would result in a non-zero EFISH signal, which is proportional to the square vertical electric field, ${E_z}^2$. We therefore conclude that the 'stray' field effect is insignificant at the present conditions, and the field is measured inside the plasma. Also, the upper bound time resolution of the present diagnostic, estimated to be ≈4 ns (see section 3.1), would be sufficient to detect the sudden electric field drop and subsequent rise, predicted by the model. We must point out that applying a single shot acquisition technique, using the HV pulse as a reference, due to the good shot-to-shot reproducibility of the breakdown moment, we improved the time resolution down to 1.7 ns, as discussed in section 3.1.

As expected, after the applied voltage is reduced back to zero, the kinetic model predicts the electric field in the gap to switch the direction (see figure 9). This is consistent with the experimental data, although the model overpredicts the peak reverse field and predicts its slower decay. The reverse field is created by the charge separation in the gap, and its decay is controlled by the neutralization of the positive and negative ions in the afterglow. Finally, the weak residual field detected before the discharge pulse is likely due to the surface charge accumulation on the dielectrics.

Further analysis of the modeling predictions indicates that the main reason for the differences between the model and the experimental results are due to two factors, (i) uncertainty in water vapor number density in the humid air, which controls the net rate of the three-body attachment in the plasma, and (ii) not accounting for the multiple ion species and ion conversion reactions, which affects the net rate of the electron-ion recombination. The modeling predictions demonstrate that the electric field in the plasma after breakdown is controlled predominantly by the rate of the electron density decay (by electron attachment and recombination, whose contributions appear to be comparable). The observed behavior of glow-like plasma emission in humid air suggests that water vapor may play a key role. Therefore, the comparison of the present experimental data with the high-fidelity simulations, including the detailed humid air chemistry and a full set of ion-molecule reactions may provide additional insight into the plasma kinetics and explain the remaining differences. An example of such simulations is the recent two-dimensional kinetic modeling predictions of streamer propagation in humid air, which incorporates the detailed ion chemistry [30].

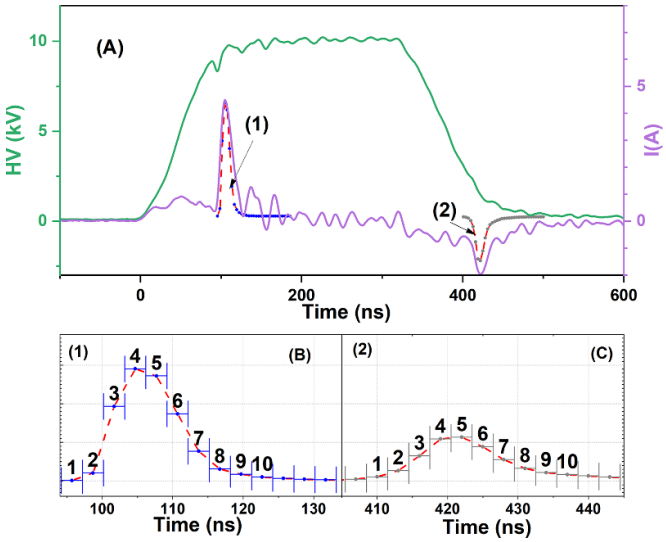

Figure 10. Gating scheme for the reported spectroscopic data. (A) Current (violette), voltage (green) and full vertical binning of spectra taken with a gate of 3 ns at the time position shown in (B) and (C) for current peak (1) and (2).

3.4. Time resolved ICCD spectra

Spatially and temporally resolved emission spectra were collected for different spectral regions. Kinetic series of spatially integrated emission over the entire discharge gap, taken with a fixed gate of 3 ns and a time step of 3 ns were performed at the discharge position using the gate scheme illustrated in figure 10. Band emission from various N_2 SPS transitions and the N_2^+ first negative system (FNS) (0,0) can be clearly identified.

The SPS and FNS bands contain interesting information on the physical parameters of the discharge. From the SPS (0,0) band the rotational temperature was derived by using the spectroscopic tool Massive OES [31–33]. Figure 11 shows the experimental SPS (0,0) averaged band profile together with synthetic profiles simulated for rotational temperatures of 314, 328, 344, 362, and 366 K respectively for the plasma induced emission observed in the corresponding gates shown in figure 10. The intensities of the FNS and SPS emission bands are determined by direct electron impact excitation processes. In weakly ionized non-equilibrium plasmas, being the mean electron energy of a few eV, only a small fraction of electrons are above the threshold for excitation processes (18.7 eV and 11.0 eV for FNS and SPS respectively). A higher threshold

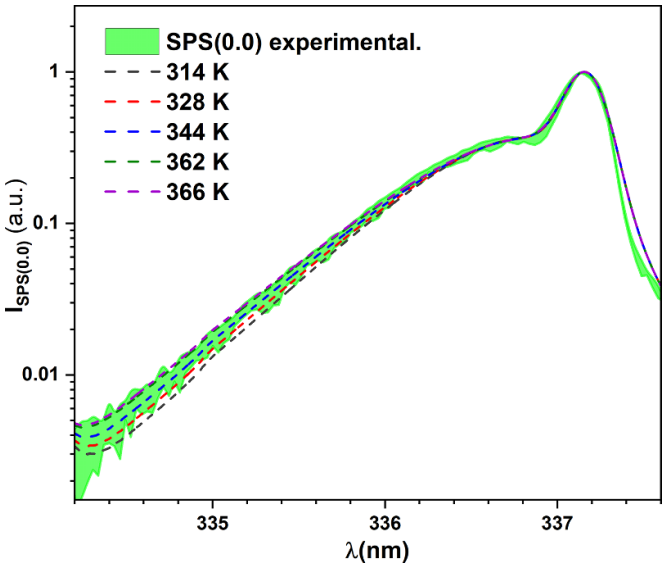

Figure 11. N_2 SPS(0,0) band emission evolution during the pulse discharge (green area), vs. simulated spectra at different temperatures during the first breakdown event.

energy is consistent with a stronger rate constant dependence on E/N [34–36].

The emission spectra during the first discharge pulse show a localized light spot at the anode, as shown at the beginning of the kinetic series (top of figure 12) that marks the end of the avalanche build-up phase. With the present time resolution and discharge time jitter it is not possible to follow the ionization wave propagation in a simple way, but the accumulated space charge causes a cathode-directed ionizing wave soon after. At the back of the ionizing wave, the electrons drift toward the anode, generating a glow near the anode. Two active zones of the discharge with different properties are formed. Near the cathode, a high electric field is present, while the density of electrons is maximal at the anode [35]. Finally, across the time interval of about 10 ns, the axial electric field is reduced due to accumulation of charge carriers on the dielectrics. This effect is clearly visible on the spectra in figure 12, with the variation of the FNS and SPS relative intensities, in time and in space. Similar behavior, with reversed polarity is observed at the HV pulse switch off (these data are not shown for the sake of simplicity).

3.5. *E/N from intensities ratio*

A widespread method to get values of the reduced electric field *E/N* in a discharge relies on the measurement of the intensity ratio of the SPS and FNS emission bands. With the proper scaling by emission probabilities, the band intensity ratios account for the population ratios of the emitting states. The connection of the populations ratios to *E/N* goes through two steps. First step, a connection with the EEDF given by the rate coefficients of the electron impact excitation process. The working hypothesis (i) for a feasible quantitative correlation is that the emitting states are excited by a single electron impact channel from the molecular ground state:

$$e + \mathrm{N_2}\left(X^1\Sigma_g^+, v'\right) \rightarrow e + \mathrm{N_2}\left(C^3\Pi_u, v\right) \rightarrow e + \mathrm{N_2}\left(B^3\Pi_g, v''\right) + h\nu_{\mathrm{SPS}} \quad (3)$$

$$e + \mathrm{N_2}\left(X^1\Sigma_g^+, v'\right) \rightarrow e + \mathrm{N_2^+}\left(B^2\Sigma_u^+, v\right) \rightarrow e + \mathrm{N_2^+}\left(X^2\Sigma_g^+, v''\right) + h\nu_{\mathrm{FNS}}. \quad (4)$$

A collision-radiative (CR) model is needed to calculate the population of the emitting states, which considers the excitation and the quenching by radiative decay and collision with surrounding molecules. At atmospheric pressure, the collision quenching is the dominant loss term of the populations.

The rate coefficients ratio can be obtained with an multiple choice of EEDFs. A realistic model is then necessary to derive an EEDF based on some physical parameters to get those that fit the ratio. The simplest case is that of a stationary condition in which the EEDF is determined by the local reduced electric field *E/N* (hypothesis (ii): local field approximation (LFA)). The second step of the procedure is then to solve the Boltzmann equation and to look for the E/N value reproducing the rate coefficients ratio. The local field hypothesis can be substituted by more complex PIC-MCC simulations allowing for non-local effects in the EEDF. In such a case the number of parameters is necessarily larger than one and the uniqueness of the interpretation of spectroscopic data may not be guaranteed.

The applicability and accuracy of this method rely on the accuracy of hypotheses (i) and (ii), and on the availability of reliable data for the excitation cross sections and quenching rate coefficients. Here, for process (1) we use the data chosen in [37], based on the cross-sections of Zubek [38, 39]. The CR model, considering the whole $\mathrm{N_2}\left(C^3\Pi_u, v\right)$ vibrational manifold, is described in [40]. For process (2) we use the excitation cross section of [41]. The collision quenching rate coefficients and vibrational relaxation are taken from [42] for $\mathrm{N_2}\left(C^3\Pi_u, v\right)$, and from [36] for $\mathrm{N_2^+}\left(X^2\Sigma_g^+, v'' = 0\right)$. A discussion on these data is out of the scope of this paper and can be found in [43]. Here we observe that large discrepancies, up to a factor of four, are found in the literature for the quenching rate coefficient of the ion B-state. Since the reason for this is not well understood, one should allow for a variation of the coefficient in the calculations.

The sample spectra with fitting are shown in figure 13. The emission bands are simulated by DIATOMIC software [44]. The spectrum is then fitted using the populations of the five $\mathrm{N_2}\left(C^3\Pi_u, v\right)$ vibrational states, used as parameters.

These populations are then fitted by the CR model in which the electron impact rate coefficients are calculated by BOLSIG+ [45] with *E/N* as a parameter (figure 13(a)), in the hypothesis of validity of the LFA, or by a mixed Maxwell–Boltzmann plus electron beam EEDF (figure 13(b), see following discussion).

The results of the electric field inferred using the spectroscopic method with LFA are shown in figure 14. The data are plotted as a function of time in the discharge pulse for three spatial positions: close to the electrodes and in the middle of the gap. The corresponding time evolution of the SPS (0,3) band is also shown, to provide the reference to the discharge pulse timing.

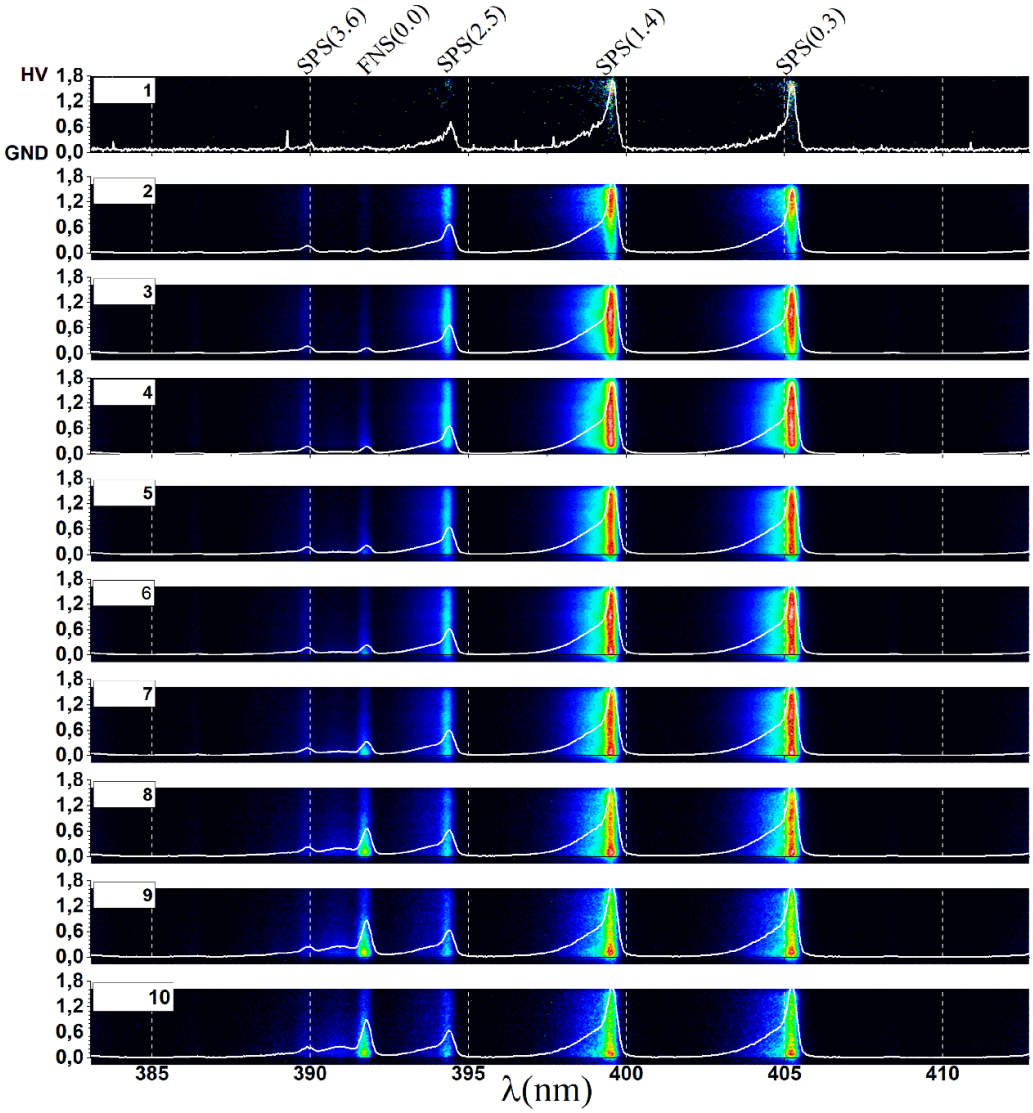

Figure 12. 1D spatially resolved spectra images for the current peak (1) at the gate position defined in panel figure 10(B). The ground electrode is located at the vertical position 0, the high voltage electrode is located at the position 1.8. In white the full vertical binning spectra derived from each image is shown to make the relative intensities of the different band emission more clearly visible. Each spectrum was normalized to the respective maximum intensities. Relative intensities at different times can be inferred from figure 10(B).

The comparison with the EFISH measurements shows a striking contrast, that is better evidenced in figure 15, where the measurements in the middle of the gap are plotted together. Here, the field values are calculated with the extreme values of the ion B-state quenching rate coefficients found in the literature (those of [36, 46]), that introduce the maximum variation in the value of the reduced electric field. Choices and uncertainties of the collisional data affect the absolute value of the *E/N* extracted from the spectroscopic measurements, but not its evolution in time (and space). In other words, the observation of an increasing field by spectroscopy, as opposed to the corresponding decrease of the field by EFISH, cannot be explained by a poor choice of the kinetic constants in the CR model.

Rather, it must be due to the incorrectness of one or both hypotheses of the method. Once the electron density decreases rapidly due to the attachment and recombination, the excitation of emitting species (N_2(C)), N_2^+(B)) may no longer be related to the *E/N* in a simple way. Regarding the hypothesis (i), in addition/competition to processes (3) and (4), other mechanisms can come into play exciting the ion B-state, that is either growing in time or decreasing less rapidly than the process (3). At this time we are not able to identify such an additional process. Electron impact processes with nitrogen ions would be competitive at charged particles densities much higher than the actual ones, not to mention that the electrons are predicted to disappear in favor of negative ions, and that certainly not all ions are molecular nitrogen. Another possibility could be vibrational energy transfer to excited states or ground state ion, but again, sufficiently high vibrational excitation which could be formed in few ns after the discharge onset appears unlikely. The breakdown of the second hypothesis would indicate the presence of a non-local contribution to the EEDF, such that a beam of fast electrons accelerated in

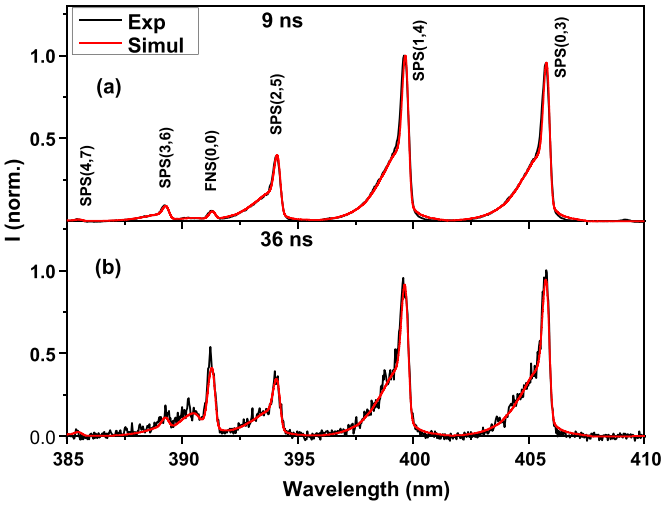

Figure 13. Spectra in the region including the $\Delta v = -3$ sequence of SPS and the (0,0) band of FNS at 9 ns and 36 ns after discharge onset. The red curve is the simulation (see text).

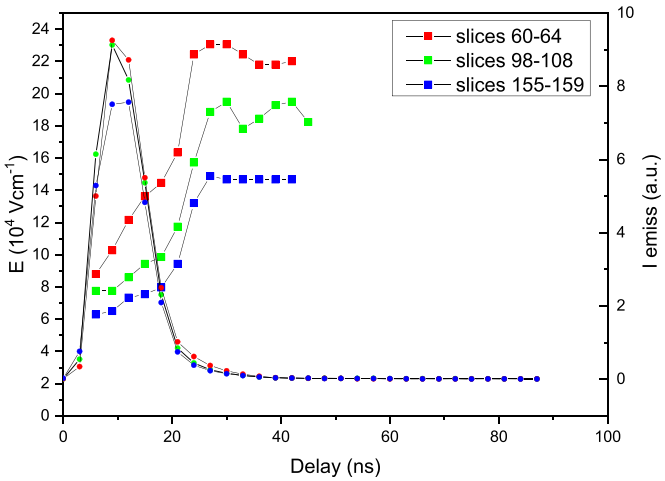

Figure 14. Electric field from the measured emission spectra in the local field approximation. Each spectrum is averaged over the specified slices of the CCD pixel array. Red and blue point refer to positions close to the cathode and anode respectively. The green points are in the middle of the gap. Circles are the corresponding intensities (band integral) of the SPS (0,3) band.

a cathode fall, giving rise to a situation similar to that found in the negative glow of a low-pressure Townsend discharge. An EEDF made of a Maxwell–Boltzmann distribution plus an e-beam contribution can in fact reproduce the spectrum at 36 ns reported in figure 13. Such a distribution is shown in figure 16. The Maxwell Boltzmann part is at a the electron temperature of 1.7 eV, corresponding to the average energy with the about 15 kV cm^{-1} electric field measured by EFISH, while the e-beam contribution is treated as an adjustable parameter. In the figure, the LFA EEDF reproducing the bands ratios is also shown, together with the plots of the electron impact cross section which give an immediate glance of why such different EEDFs can produce the same bands ratios.

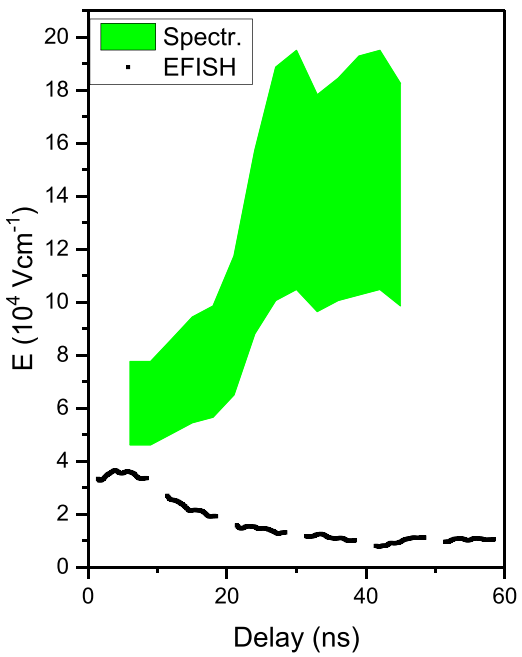

Figure 15. Electric field by EFISH (black) and by the spectroscopic method (green) with extreme values of the collision quenching rate coefficients of $N_2^+\left(X^2\Sigma_g^+, v'' = 0\right)$ .U upper limit: k = 8.8 × 10^{-10} cm^3 s^{-1} (N_2) and k = 10.45 × 10^{-10} cm^3 s^{-1} (O_2) [36]. Lower limit k = 2.1 × 10^{-10} cm^3 s^{-1}(N_2) and k = 5.1 × 10^{-10} cm^3 s^{-1} (O_2) and [46].

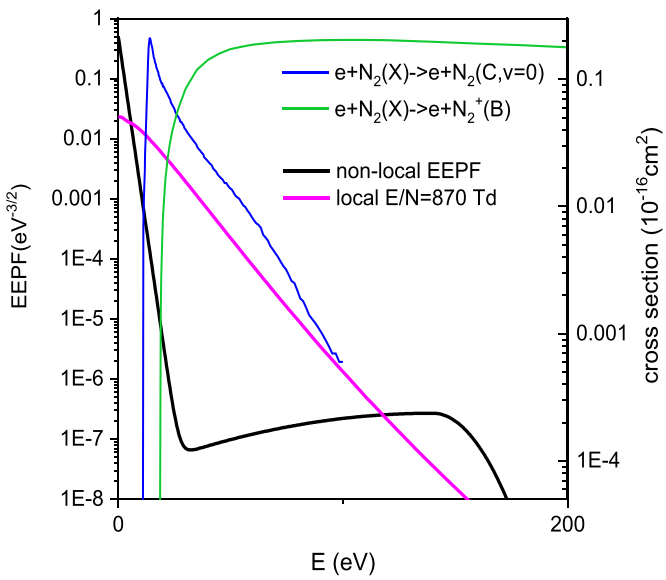

Figure 16. EEPF (EEDF/energy $^{1/2}$) corresponding to the fitting of figure 6.1(b) spectrum. Magenta: local E/N, black: non-local EEDF (see text). Blue and green curves are the cross sections of processes (1) and (2).

Needless to say, multiple combinations of non-local EEDF shapes such as plotted in figure 16 can yield the same emission bands ratio. The one in figure 16 is given as an illustration of the breakdown of the non-local hypothesis, which physically corresponds to the formation and growth in time of a space

charge structure in the gap resembling that of a DC low pressure one. The verification of this conjecture must be deferred to the detailed modeling, e.g. using the PIC-MCC simulations, capable of accounting for the non-local effects.

We finally conclude that at the present discharge conditions, the spectroscopic measurement of *E/N* does not yield accurate results. Such a conclusion has been made possible by the combination of independent time and space resolved measurement of both nitrogen emission spectra and of the electric field.

4. Conclusions

In summary, the comparison of the absolute, time-resolved measurements of the electric field in a plane-to-plane, ns pulse, dielectric barrier discharge in humid air with the kinetic modeling predictions revealed new features which have not been observed previously in non-electronegative gas mixtures. The first feature is a strong electric field in the plasma established after the ns pulse breakdown. Unlike in electropositive plasmas, the rapid conversion of electrons to negative ions after breakdown, on a nanosecond time scale, greatly retards their transport and 'preserves' the space charge distribution in the gap after breakdown. The second feature is the gradual decay of the electric field in the afterglow, caused by the relatively slow ion transport in the ion-ion plasma. In electropositive plasmas, the residual electric field reduction in the afterglow is much faster, due to the much higher mobility of electrons.

Future work will focus on obtaining the additional experimental data and exercising the kinetic model over a wide range of discharge parameters, such as the peak applied voltage, voltage rise/fall time, pulse duration, and mixture composition. This will provide additional insight into the underlying kinetic processes controlling the electric field distributions in high-pressure plasmas generated in ns pulse discharges.

Data availability statement

All data that support the findings of this study are included within the article (and any supplementary files).

Acknowledgments

I V A Acknowledge the financial support of the CNR STM 2019 programme for funding his stay at ISTP in Bari.

D A and P F A Acknowledge the Project 'Plasma Reactors for Agrifood industry (PlasmaReA)' b5667f07, in the framework of POC PUGLIA FESRT-FSE 2014/2020 Fondo Sociale Europeo (C(2015)5854 del 13/08/2015) Riparti (assegni di Ricerca per riPARTire con le imprese).

Funding

PONa3_00369 SISTEMA, and by the Italian Ministry of Economic Development (MISE), PON FESR 2014–2020, Grant Number Protection F/050421/01-03/X32.

ORCID iDs

Paolo F Ambrico https://orcid.org/0000-0002-2455-6949
Domenico Aceto https://orcid.org/0000-0002-5748-8962
Xin Yang https://orcid.org/0000-0003-1723-6039
Giorgio Dilecce https://orcid.org/0000-0001-5808-1868
Marianna Ambrico https://orcid.org/0000-0002-0568-6860
Ivo Furno https://orcid.org/0000-0001-8348-1716
Igor V Adamovich https://orcid.org/0000-0001-6311-3940

References

[1] Ambrico P F, Šimek M, Ambrico M, Morano M, Prukner V, Minafra A, Allegretta I, Porfido C, Senesi G S and Terzano R 2020 On the air atmospheric pressure plasma treatment effect on the physiology, germination and seedlings of basil seeds *J. Phys. D: Appl. Phys.* **53** 104001

[2] Ambrico P F, Šimek M, Rotolo C, Morano M, Minafra A, Ambrico M, Pollastro S, Gerin D, Faretra F and De Miccolis Angelini R M 2020 Surface dielectric barrier discharge plasma: a suitable measure against fungal plant pathogens *Sci. Rep.* **10** 1–17

[3] Ambrico P F, Šimek M, Morano M, De Miccolis Angelini R M, Minafra A, Trotti P, Ambrico M, Prukner V and Faretra F 2017 Reduction of microbial contamination and improvement of germination of sweet basil (Ocimum basilicum L.) seeds via surface dielectric barrier discharge *J. Phys. D: Appl. Phys.* **50** 305401

[4] Patil S, Bourke P and Cullen P J J 2016 *Principles of Nonthermal Plasma Decontamination* (Elsevier Inc.)

[5] Scholtz V, Pazlarova J, Souskova H, Khun J and Julak J 2015 Nonthermal plasma—a tool for decontamination and disinfection *Biotechnol. Adv.* **33** 1108–19

[6] Ehlbeck J, Schnabel U, Polak M, Winter J, von Woedtke T, Brandenburg R, von Dem Hagen T and Weltmann K-D 2010 Low temperature atmospheric pressure plasma sources for microbial decontamination *J. Phys. D: Appl. Phys.* **44** 013002

[7] Pignata C, D'Angelo D, Fea E and Gilli G 2017 A review on microbiological decontamination of fresh produce with nonthermal plasma *J. Appl. Microbiol.* **122** 1438–55

[8] Waskow A, Howling A and Furno I 2021 Mechanisms of plasma-seed treatments as a potential seed processing technology *Front. Phys.* **9** 617345

[9] Dogariu A, Goldberg B M, O'Byrne S and Miles R B 2017 Species-independent femtosecond localized electric field measurement *Phys. Rev. Appl.* **7** 024024

[10] Goldberg B M, Chng T L, Dogariu A and Miles R B 2018 Electric field measurements in a near atmospheric pressure nanosecond pulse discharge with picosecond electric field induced second harmonic generation *Appl. Phys. Lett.* **112** 064102

[11] Simeni Simeni M, Tang Y, Frederickson K and Adamovich I V 2018 Electric field distribution in a surface plasma flow actuator powered by ns discharge pulse trains *Plasma Sources Sci. Technol.* **27** 104001

[12] Chng T L, Orel I S, Starikovskaia S M and Adamovich I V 2019 Electric field induced second harmonic (E-FISH) generation for characterization of fast ionization wave discharges at moderate and low pressures *Plasma Sources Sci. Technol.* **28** 045004

[13] Chng T L, Brisset A, Jeanney P, Starikovskaia S M, Adamovich I V and Tardiveau P 2019 Electric field

evolution in a diffuse ionization wave nanosecond pulse discharge in atmospheric pressure air *Plasma Sources Sci. Technol.* **28** 09LT02

[14] Simeni Simeni M, Tang Y, Hung Y-C, Eckert Z, Frederickson K and Adamovich I V 2018 Electric field in Ns pulse and AC electric discharges in a hydrogen diffusion flame *Combust. Flame* **197** 254–64

[15] Tang Y, Simeni Simeni M, Frederickson K, Yao Q and Adamovich I V 2019 Counterflow diffusion flame oscillations induced by ns pulse electric discharge waveforms *Combust. Flame* **206** 239–48

[16] Goldberg B M, Reuter S, Dogariu A and Miles R B 2019 1D time evolving electric field profile measurements with sub-ns resolution using the E-FISH method *Opt. Lett.* **44** 3853

[17] Bigio I J, Finn R S and Ward J F 1975 Electric-field induced harmonic generation as a probe of the focal region of a laser beam *Appl. Opt.* **14** 336

[18] Adamovich I V, Butterworth T, Orriere T, Pai D Z, Lacoste D A and Cha M S 2020 Nanosecond second harmonic generation for electric field measurements with temporal resolution shorter than laser pulse duration *J. Phys. D: Appl. Phys.* **53** 145201

[19] Obrusník A, Bílek P, Hoder T T, Šimek M, Bonaventura Z, Obrusnik A, Bilek P, Hoder T T, Šimek M and Bonaventura Z 2018 Electric field determination in air plasmas from intensity ratio of nitrogen spectral bands: i. Sensitivity analysis and uncertainty quantification of dominant processes *Plasma Sources Sci. Technol.* **27** 085013

[20] Chng T L, Starikovskaia S M and Schanne-Klein M-C 2020 Electric field measurements in plasmas: how focusing strongly distorts the E-FISH signal *Plasma Sources Sci. Technol.* **29** 125002

[21] Orr K, Yang X, Gulko I and Adamovich I V 2020 Formation and propagation of ionization waves during ns pulse breakdown in plane-to-plane geometry *Plasma Sources Sci. Technol.* **29** 125022

[22] Pitchford L C *et al* 2017 LXCat: an open-access, web-based platform for data needed for modeling low temperature plasmas *Plasma Process. Polym.* **14** 1600098

[23] Aleksandrov N L, Bazelyan E M, Ponomarev A A and Starikovsky A Y 2022 Kinetics of charged species in non-equilibrium plasma in water vapor- and hydrocarbon-containing gaseous mixtures *J. Phys. D: Appl. Phys.* **55** 383002

[24] Aleksandrov A F, Bychkov V L, Grachev L P, Esakov I I and Lomteva A Y 2006 Air ionization in a near-critical electric field *Tech. Phys.* **51** 330–5

[25] Van Gaens W and Bogaerts A 2014 Corrigendum: kinetic modelling for an atmospheric pressure argon plasma jet in humid air (J. Phys. D: Appl. Phys. 46 (2013) 275201) *J. Phys. D: Appl. Phys.* **47** 079502

[26] Ellis H W, McDaniel E W, Albritton D L, Viehland L A, Lin S L and Mason E A 1978 Transport properties of gaseous ions over a wide energy range. Part II *At. Data Nucl. Data Tables* **22** 179–217

[27] Ellis H W, Pai R Y, McDaniel E W, Mason E A and Viehland L A 1976 Transport properties of gaseous ions over a wide energy range *At. Data Nucl. Data Tables* **17** 177–210

[28] Raizer Y P 1991 *Gas Discharge* (Springer) ch 5

[29] Huang B, Zhang C, Adamovich I, Akishev Y and Shao T 2020 Surface ionization wave propagation in the nanosecond pulsed surface dielectric barrier discharge: the influence of dielectric material and pulse repetition rate *Plasma Sources Sci. Technol.* **29** 044001

[30] Starikovskiy A, Bazelyan E and Aleksandrov N 2023 The effect of humidity on streamer propagation in long air gaps *AIAA SCITECH 2023 Forum* (American Institute of Aeronautics and Astronautics) (https://doi.org/10.2514/6.2023-1867)

[31] Voráč J, Synek P, Procházka V and Hoder T 2017 State-by-state emission spectra fitting for non-equilibrium plasmas: OH spectra of surface barrier discharge at argon/water interface *J. Phys. D: Appl. Phys.* **50** 294002

[32] Voráč J, Synek P, Potočňáková L, Hnilica J and Kudrle V 2017 Batch processing of overlapping molecular spectra as a tool for spatio-temporal diagnostics of power modulated microwave plasma jet *Plasma Sources Sci. Technol.* **26** 025010

[33] Voráč J, Kusýn L and Synek P 2019 Deducing rotational quantum-state distributions from overlapping molecular spectra *Rev. Sci. Instrum.* **90** 123102

[34] Simek M 2014 Optical diagnostics of streamer discharges in atmospheric gases *J. Phys. D: Appl. Phys.* **47** 463001

[35] Hoder T, Bonaventura Z, Bourdon A and Simek M 2015 Picosecond delays of light emitted by streamer in atmospheric pressure air: analysis of $N_2(C^3\prod_u)$ and N_2^+ $(B^2\sum_u{}^+)$ emissions and fundamental streamer structure *J. Appl. Phys.* **117** 073302

[36] Dilecce G, Ambrico P F and De Benedictis S 2010 On the collision quenching of $N_2^+(B^2\sum_u{}^+$, v=0) by N_2 and O_2 and its influence on the measurement of E/N by intensity ratio of nitrogen spectral bands *J. Phys. D: Appl. Phys.* **43** 195201

[37] Šimek M 2002 The modelling of streamer-induced emission in atmospheric pressure, pulsed positive corona discharge: N_2 second positive and NO-γ systems *J. Phys. D: Appl. Phys.* **35** 1967–80

[38] Zubek M 1994 Excitation of the C^3Pi_u state of N_2 by electron impact in the near-threshold region *J. Phys. B: At. Mol. Opt. Phys.* **27** 573–81

[39] Zubek M and King G C 1994 Differential cross sections for electron impact excitation of the C ^3Pi_u, E $^3\sum_g{}^+$ and a" $^1\sum_g{}^+$ states of N_2 *J. Phys. B: At. Mol. Opt. Phys.* **27** 2613–24

[40] Dilecce G, Ambrico P F, Martini L M and Tosi P 2022 On the determination of the vibrational temperature by optical emission spectroscopy *Plasma Sources Sci. Technol.* **31** 077001

[41] Borst W L and Zipf E C 1970 Cross section for electron-impact excitation of the (0,0) first negative band of N_2^+ from threshold to 3 keV *Phys Rev A* **1** 834–40

[42] Dilecce G, Ambrico P F and De Benedictis S 2006 OODR-LIF direct measurement of $N_2(C\ ^3\Pi_u$, v=0–4) electronic quenching and vibrational relaxation rate coefficients by N_2 collision *Chem. Phys. Lett.* **431** 241–6

[43] Dilecce G 2014 Optical spectroscopy diagnostics of discharges at atmospheric pressure *Plasma Sources Sci. Technol.* **23** 015011

[44] Tan X 2006 Diatomic, a spectral simulation program for diatomic molecules on windows platforms, release 1.292 technical report (Department of Chemistry, The Johns Hopkins University)

[45] Hagelaar G J M and Pitchford L C 2005 Solving the Boltzmann equation to obtain electron transport coefficients and rate coefficients for fluid models *Plasma Sources Sci. Technol.* **14** 722–33

[46] Pancheshnyi S V, Starikovskaia S M and Starikovskii A Y 1998 Measurements of rate constants of the $N_2(C^3\Pi_u$,v′=0) and $N_2^+(B^2\Sigma^+{}_u$,v′=0) deactivation by N_2, O_2, H_2, CO and H_2O molecules in afterglow of the nanosecond discharge *Chem. Phys. Lett.* **294** 523–7